Fuel-flexible operation of a solid oxide fuel cell with $Sr_{0.8}La_{0.2}TiO_3$ support

Manoj R. Pillai [a,b], Ilwon Kim [b], David M. Bierschenk [a], Scott A. Barnett [a,*]

[a] Department of Materials Science and Engineering, Northwestern University, Evanston, IL 60208, USA
[b] Functional Coating Technology, Evanston, IL 60201, USA

ARTICLE INFO

ABSTRACT

Solid oxide fuel cells with $Sr_{0.8}La_{0.2}TiO_3$ anode-side supports, Ni- Sm-doped ceria adhesion layer, Ni- Y_2O_3-stabilized ZrO_2 (YSZ) anode active layer, YSZ electrolyte, and $La_{0.8}Sr_{0.2}MnO_3$(LSM)–YSZ cathode are described. These cells are stable in simulated natural gas at current densities as low as $0.2\,A\,cm^{-2}$. This represents much-improved stability against coking in natural gas, compared with conventional Ni–YSZ anode-supported SOFCs which rapidly coke, even at higher current densities. Cell operation in H_2 fuel with 50–100 ppm, H_2S results in an initial decrease in cell power density, but no long-term degradation occurs and full recovery to the initial performance level is observed after dry H_2 fuel flow is restored. Degradation is not observed during or after seven redox cycles between H_2 and air.

© 2008 Elsevier B.V. All rights reserved.

1. Introduction

A Ni- Y_2O_3-stabilized ZrO_2 (Ni–YSZ) cermet is used as both the anode and mechanical support in many solid oxide fuel cells (SOFCs). However, Ni–YSZ imposes significant limitations on the fuels that can be utilized due to susceptibility to coking in hydrocarbon fuels, poisoning by sulfur impurities, and degradation upon repeated anode exposure to air [1]. A number of strategies have been investigated to overcome these limitations, including alternate anode materials and cell designs. New anode materials are typically electronically conducting oxides, in some cases combined with a non-Ni metallic phase [2–4]. Recent examples that have provided good electrochemical performance include $Sr_2Mg_{1-x}Mn_xMoO_{6-\delta}$ ($x = 0–1$) [5], $La_{0.75}Sr_{0.25}Cr_{0.5}Mn_{0.5}O_3$ (with a $Ce_{0.8}Gd_{0.2}O_{2-\delta}$ interlayer) [6] and (La,Sr)(Ti,Ce)O_3 [7]. Even though measured anode polarization resistances are consistent with cell power density of $\sim 1\,W\,cm^{-2}$ in some cases the oxide anodes are typically implemented in SOFCs with thick self-supporting electrolytes, limiting power densities to values substantially less than $1\,W\,cm^{-2}$, as often achieved with thin-electrolyte Ni–YSZ anode-supported SOFCs. The use of oxide anodes in conventional co-sintered anode-supported SOFCs is difficult or impossible because of potential microstructural coarsening and/or interdiffusion/reactions between the anode and electrolyte.

New cell designs or process schemes have the potential to overcome these difficulties. For example, infiltration of porous anodes can be utilized to introduce new anode active-layer materials after the high-temperature co-sintering is completed [1,8,9]. Similarly, thin-electrolyte cathode-supported SOFCs allow anode application and firing after high-temperature co-sintering [10]. A different strategy, that has been employed to improve the coking resistance of Ni–YSZ-anode-supported cells operated in methane, is the addition of a porous, non-coking barrier layer at the anode [11–14]. However, the cell-barrier combination remains susceptible to coking unless a substantial cell current density is maintained, and the separate barrier layer increases concentration polarization and complicates stack design. A new cell design, where a conducting oxide material is used as the cell anode-side support and built-in barrier layer, was recently reported to provide much-improved stability in methane fuel [15].

Here we describe further results on these oxide anode-side supported SOFCs. As in the prior report, the conducting support is $Sr_{0.8}La_{0.2}TiO_3$ (SLT) and the electrochemically active anode layer is Ni–YSZ. SLT has been successfully used as a current collector [16], ceramic anode [17], and as a component with YSZ in a support framework [8] for SOFCs. The materials properties of SLT make it a good candidate support for an SOFC. SLT has been reported to be stable over the wide range of oxygen partial pressures and temperatures expected under typical SOFC operating conditions, and to not react significantly with other SOFC materials [17–19]. The average thermal expansion coefficient in the temperature range 50–1000 °C is $(11–12) \times 10^{-6}\,K^{-1}$, between the values for YSZ and

* Corresponding author. Tel.: +1 847 491 2447; fax: +1 847 491 7820.
E-mail address: s-barnett@northwestern.edu (S.A. Barnett).

Ni–YSZ, and varies only slightly with oxygen partial pressure (>0.1% from $pO_2 = 10^{-18}$ to 0.2 atm) [17]. The present composition with 20% La was chosen based on a preliminary study in which this composition showed the highest conductivity at 800 °C in humidified hydrogen (samples initially fired in air): 10 S cm^{-1}. The Ni–YSZ anode active layer helps yield power densities of up to 1 W cm^{-2} at 800 °C, similar to conventional Ni–YSZ-supported SOFCs. The SOFCs were prepared using a co-sinter processing route similar to that used for Ni–YSZ anode-supported cells. Results on sulfur tolerance, redox cycling, and stability in simulated natural gas are presented.

2. Experimental procedure

The present SOFCs had SLT anode supports instead of Ni–YSZ, but the thick-film electrochemically active layers were the same as in conventional SOFCs[1]—Ni–YSZ anode, YSZ electrolyte, and $La_{0.8}Sr_{0.2}MnO_3$ (LSM)–YSZ cathode. $SrCO_3$, La_2O_3 and TiO_2 powders were mixed together in an appropriate weight ratio and calcined at 950 °C to obtain $Sr_{0.8}La_{0.2}TiO_3$. X-ray powder diffractometer scans were very similar to those reported in Ref. [17] for this composition, showing only peaks characteristic of the intended $Sr_{0.8}La_{0.2}TiO_3$ perovskite phase. The SLT powder was then mixed with 20 wt.% carbon pore former and wet ball milled for 24 h. The resulting slurry was dried and sieved. The powder was die pressed into 19 mm diameter pellets weighing 0.4–0.5 g. The pellets were pre-fired at 1320 °C for 4 h to burn off the carbon and also to achieve some structural strength for further processing.

A colloidal deposition technique was used to apply the electrochemically active, thick-film layers. Colloidal solutions of $NiO–Ce_{0.8}Sm_{0.2}O_2$(SDC) (1:1 by weight), NiO–YSZ (1:1 by weight), and YSZ were prepared by mixing the powders with ethanol, poly(vinyl butyral) (PVB) as binder, ethyl cellulose, and polyethylenimine (PEI) as dispersant. Commercial NiO (<3 μm, J.T. Baker), YSZ (~200 nm, Tosoh), and SDC (Nex Tech) were used. The solutions were ball milled for 24 h for thorough mixing. The colloidal solutions of NiO–SDC, NiO–YSZ, and YSZ were sequentially drop coated onto the SLT pellets, with a 1000 °C, 1 h firing step between each coating. The NiO–SDC layer was used to improve adhesion and to help prevent interdiffusion or reactions between the SLT support and the NiO–YSZ anode active layer. After the NiO–SDC, NiO–YSZ, and YSZ electrolyte coating steps, the structures were co-fired at 1420 °C for 4 h to ensure a fully dense electrolyte. Finally, the cathode layers were applied either by screen printing or by doctor blading. The inks were prepared by mixing the appropriate powders with a vehicle (V-737, Heraeus Inc., PA) in a three-roll mill. The cathode active layer consisting of an LSM–YSZ mixture (1:1 by weight) was applied and then fired at 1175 °C for 1 h, followed by a layer of LSM that was fired at 1125 °C for 1 h. A silver current collection grid was painted on each cell using Ag ink (DAD-87, Shanghai Research Institute of Synthetic Resin).

The resulting cells had a final thickness of ~0.7–0.8 mm and a diameter of ~15 mm. The cathode surface area on each cell was 0.5 cm^2. Archimedes measurements showed that the SLT supports had a porosity of ~40%. Fabrication details for Ni–YSZ anode-supported cells have been described previously [12]. The Ni–YSZ anode-supported cells used in this study were fabricated to have a similar thickness (~7 mm) and diameter (~15 mm) as the SLT supported cells. The thick-film cathode active layer and cathode current collector were prepared as described above for the SLT-supported cells.

The anode-side support of each button cell was sealed to an alumina support tube using Ag ink and fuel was supplied via a smaller, second alumina tube concentric with the support tube.

Electrical contacts were attached using Ag ink in the standard four-probe configuration. The cathode was exposed to ambient air. Temperature was measured with a thermocouple placed in contact with the cathode. During initial cell heating, dry hydrogen was supplied in order to reduce the anode NiO to Ni. After anode reduction, the cell testing was initiated. Current–voltage and electrochemical impedance spectroscopy (EIS) curves were measured using an Electrochemical Workstation (IM6, ZAHNER). The frequency range for the impedance measurements was 0.1–1 MHz. Constant current voltage measurements were taken using a Keithley 2420 sourcemeter. The cell structure was observed after testing using scanning electron microscopy (SEM) in a Hitachi S-3400N-II microscope fitted with an Oxford energy dispersive X-ray spectrometer. The surrogate natural gas mixture (airgas) used in this study contained 5% propane, 10% ethane, and balance methane. H_2S laden hydrogen mixtures were prepared by mixing pure H_2 (airgas) and H_2 containing 300 ppm H_2S (BOC Gases) using mass flow controllers.

3. Results and discussion

3.1. Structural and chemical evaluation

Fig. 1 shows a typical energy dispersive X-ray spectroscopy (EDS) spectrum taken from the Ni–YSZ and Ni–SDC layers of a typical cell after electrical testing. The Ni–YSZ and Ni–SDC layers were of particular interest because contamination from the SLT support, due to diffusion during high-temperature co-firing, could potentially affect anode electrochemical properties. There was a small apparent peak at ~4.5 keV that might indicate a low level (near the EDS detection limit of 0.1–1%) of Ti. The overlap between the Zr, Y, and Sr peaks makes it impossible to conclude whether there was any Sr in the anode active layer.

Fig. 2 shows a typical fracture cross-sectional SEM image and EDS chemical maps from a typical SLT-supported cell after testing. The energy ranges used for compiling the EDS element maps are illustrated in Fig. 1. The SEM image shows the expected structure with a dense YSZ layer, porous cathode, and porous anode active layers. The SLT support shows large spherical pores from the carbon pore former. The EDS maps showed that the elements were mostly confined within their respective layers, except for artifacts arising from peak overlaps. Zr and Y appeared primarily in the YSZ, Ni–YSZ, and LSM–YSZ layers, as expected. While considerable Zr and Y intensity was also observed in the SLT support, this was an artifact resulting from overlap between the Sr, Y, and Zr EDS peaks. Similarly, Sr and Ti were mainly in the SLT layer, as expected, but there was some Sr intensity in the YSZ layer due to Sr–Zr–Y
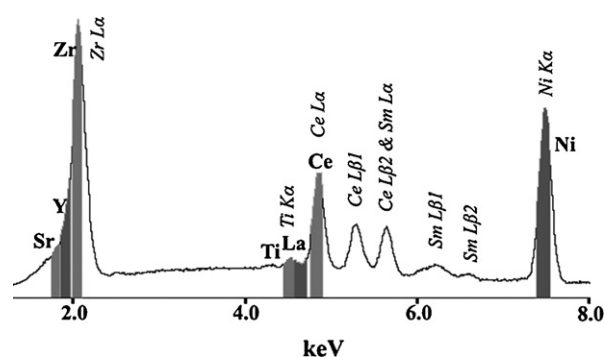

Fig. 1. EDS spectrum taken from the Ni–SDC and Ni–YSZ layers of a typical cell after electrical testing. Energy windows used to form the EDS element maps in Fig. 2 are indicated by the shaded regions.
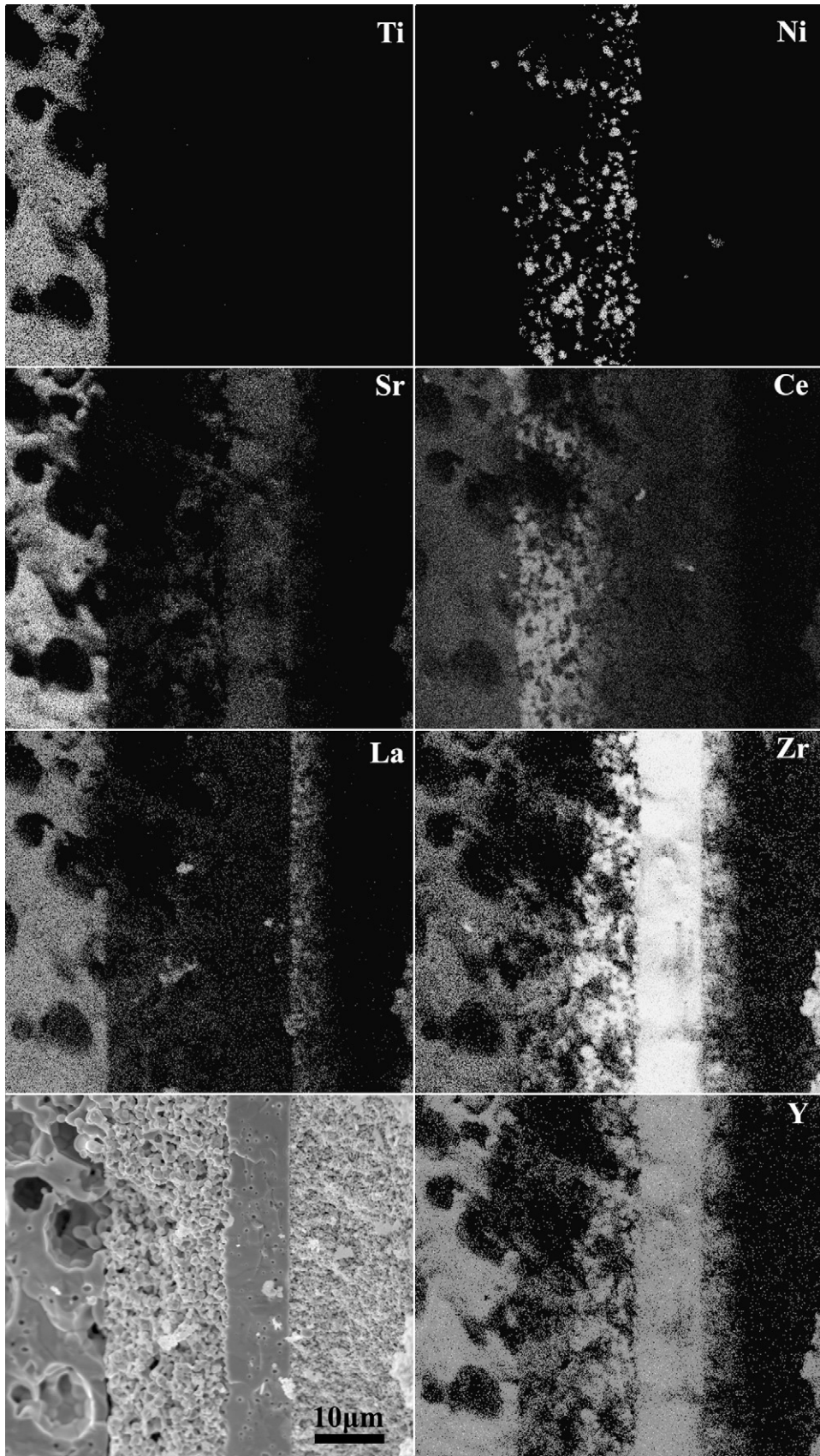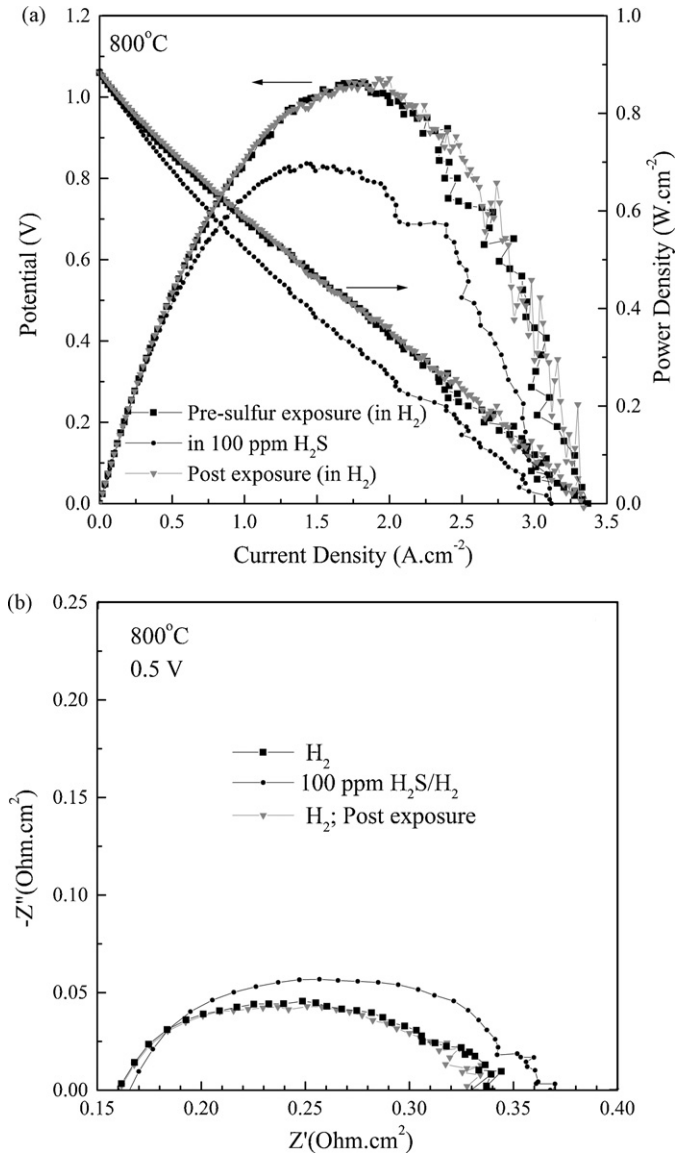
Fig. 2. SEM image and Ti, Sr, La, Ni, Ce, Zr, and Y EDS element maps from a fracture cross-section of a typical cell after electrical testing.

Fig. 3. (a) Voltage and power density versus current density and (b) electrochemical impedance spectra obtained from an SLT-supported SOFC at 800 °C. Results are shown for dry H_2 fuel prior to H_2S exposure, in H_2 with 100 ppm H_2S, and in dry H_2 after the H_2S exposure.

steady-state operation. We discuss first the results for dry H_2 fuel. The open circuit voltage was 1.07 V and the maximum power density was 0.85 W cm^{-2}. Similar results were reported previously, and data shown for operating temperatures from 600 to 800 °C indicated the typical decrease in power density with decreasing temperature [15]. The dry-H_2 EIS data indicate approximately equal components of ohmic (0.16 Ω cm^2) and polarization (0.17 Ω cm^2) resistances. The ohmic component was due mainly to the YSZ electrolyte resistance, which is expected to be $\approx$0.1 Ω cm^2 for the present $\sim$10 μm thick electrolytes [20], but there was also a component from the resistance of the SLT support, which contributed $\sim$0.02 Ω cm^2 [15]. There was a single depressed arc that included contributions from both the anode and cathode polarization; it was previously shown that the polarization resistance was larger by $\sim$0.03 Ω cm^2 for SLT-supported versus Ni–YSZ-supported SOFCs. The present EDS results (Fig. 1) suggest that there may be a trace amount of Ti or other elements from the support that diffuse into the Ni–YSZ active layer during processing, thereby affecting the anode polarization resistance.
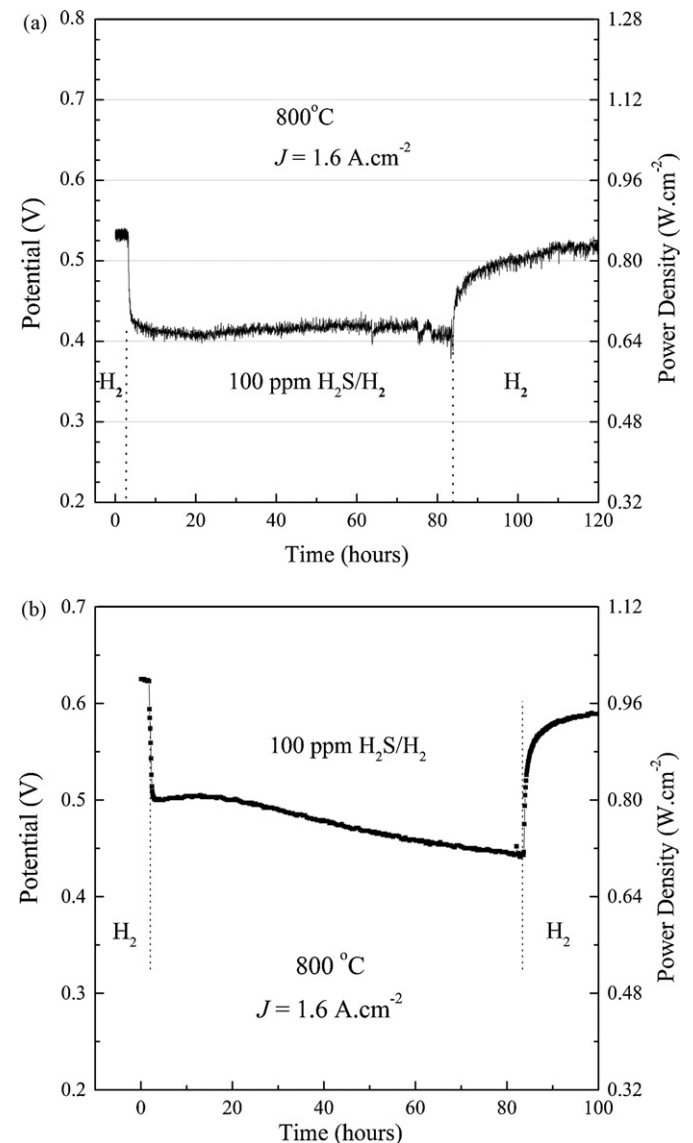
peak overlap. The Ce that appears to be present in the SLT support is an artifact resulting from the overlap between Ti, La and Ce.

Additional EDS spectra from the SLT support (not shown here) provided strong evidence that Ce, Zr, Y and Sm were, indeed, confined to the anode functional layer. On the other hand, low levels of Ni were detected in the SLT support near the Ni-containing layers. Additional SEM images of the SLT support showed that the region near the Ni-containing layers was more dense than in the remainder of the support, suggesting that SLT sintering was enhanced by the presence of this Ni impurity.

3.2. Electrical characterization with H_2 fuel

Fig. 3 shows current–voltage (a) and EIS (b) results from a typical SLT-supported cell operated at 800 °C in dry H_2, H_2 with 100 ppm H_2S, and then after the fuel was switched back to dry H_2. In each case, the measurements were made after the cell had reached

Fig. 4. Voltage versus time for (a) SLT-supported and (b) Ni–YSZ-supported SOFCs tested at 1.6 A cm^{-2} and 800 °C in dry H_2 and H_2 with 100 ppm H_2S.

3.3. Sulfur tolerance

In Fig. 3, the current–voltage curves showed a higher cell resistance in the fuel with 100 ppm H_2S, resulting in a decrease in the maximum power density to $\approx 0.7\,W\,cm^{-2}$. The EIS data showed that the resistance increase was $0.04\,\Omega\,cm^2$, and was due entirely to increased polarization resistance. After the fuel flow was changed back to dry hydrogen, the cell characteristics returned to their initial values.

Fig. 4 shows results from constant-current tests with 100 ppm H_2S in H_2 fuel, comparing SLT– and Ni–YSZ-supported SOFCs. For the SLT-supported cell (Fig. 4a), there was an initial ~100 mV drop upon H_2S exposure, but the cell voltage remained stable within $\approx 20\,mV$ thereafter. The cell recovered to nearly its initial voltage when the H_2S was removed (longer recoveries done in other cell tests showed complete recovery). For a Ni–YSZ cell (Fig. 4b), the initial voltage drop was slightly larger, $\approx 120\,mV$, and there was an additional continuous decrease in voltage from 500 to 430 mV over 70 h. Zha et al. [21] have suggested that the long-term degradation is caused by a change in the Ni surface reconstruction due to S adsorption, which in turn causes Ni surface planes to gradually shift to less electrochemically active orientations. Given that the present SLT-supported cells featured Ni–YSZ anode active layers, this degradation mechanism should have been operative, and yet the cells did not exhibit long-term degradation. There may have been an effect of the ceria present in the present anodes, as ceria has been shown to positively impact sulfur tolerance [22]. Alternatively, the present results may indicate that the anode support plays an important, but as yet unknown, role in sulfur tolerance.

Fig. 5 shows the effect of different H_2S concentrations on the cell performance. The cell voltage at $J = 1.6\,A\,cm^{-2}$ dropped from 535 mV in dry H_2 to ~460 mV in 50 ppm H_2S to ~430 mV in 100 ppm H_2S to ~390 mV in 300 ppm H_2S. This trend is similar to that observed for Ni–YSZ-supported SOFCs [21,23], and is presumably related to increasing contaminant adsorption on anode surfaces. The voltage appears to stabilize rapidly at 50 ppm, whereas for 100 and 300 ppm the voltage is decreasing over the 5–8 h measurement period. The results shown in Fig. 4a indicate that the performance eventually stabilized for 100 ppm, but it is not known if the cells would stabilize at 300 ppm. In all cases, the cell voltage recovered to nearly the initial voltage of 530 mV when the fuel was switched
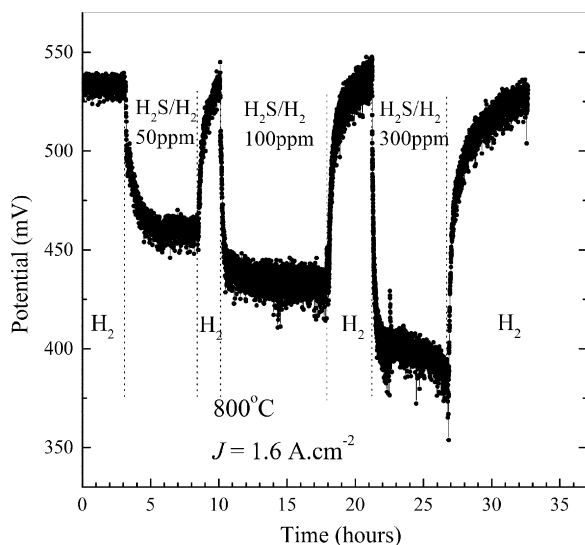

Fig. 5. Voltage versus time for a cell operated at 800 °C and $J = 1.6\,A\,cm^{-2}$ in either dry hydrogen or hydrogen with 50, 100, or 300 ppm H_2S.

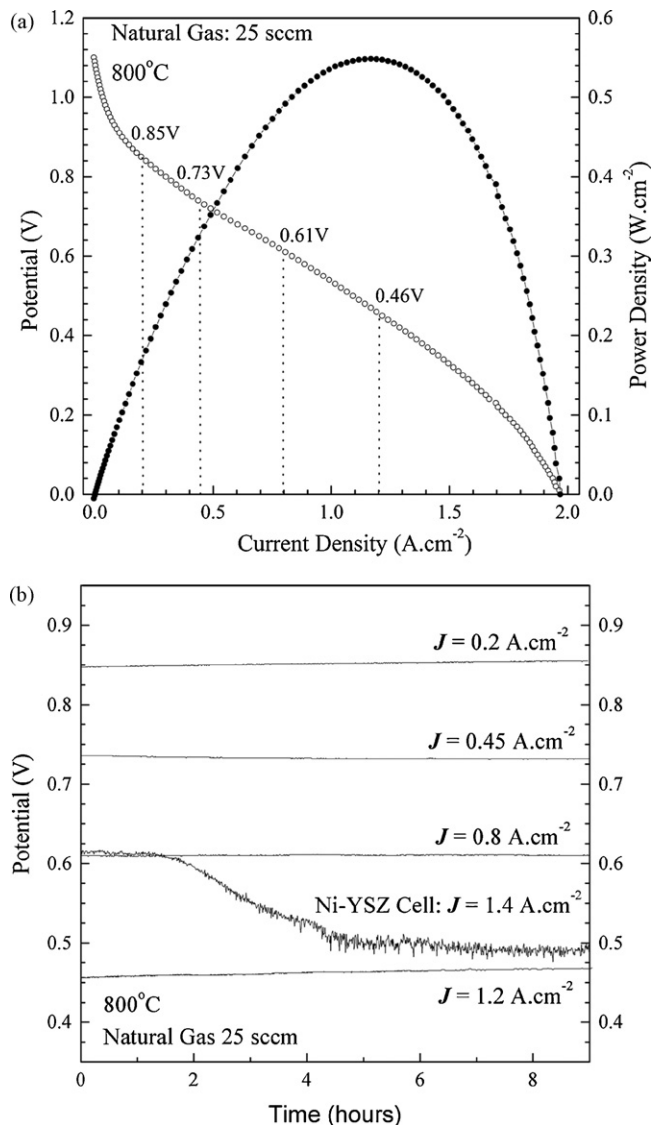**Fig. 6.** (a) Voltage and power density versus current density from an SLT-supported cell tested in natural gas at 800 °C. (b) Cell voltage versus time at different current densities while testing the cell in natural gas at 800 °C. Voltage versus time for a Ni–YSZ-supported cell operated in natural gas at 800 °C and 1.4 A cm^{-2} is shown for comparison.

back to dry H_2, although the recovery was slower after dosing with higher H_2S concentrations.
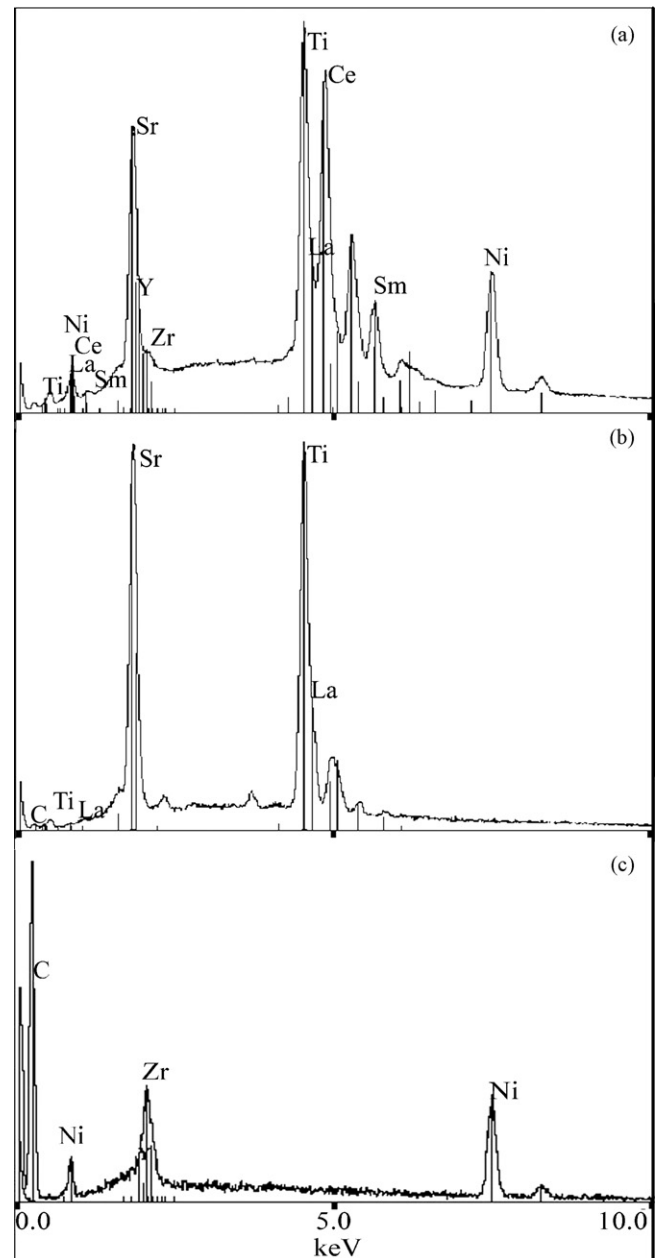
3.4. Natural gas testing

Fig. 6a shows a typical set of current–voltage results at 800 °C from an SLT-supported cell fed with a synthetic natural gas fuel: 85% methane, 10% ethane, and 5% propane. This fuel had higher levels of ethane and propane than found in typical natural gas—~7% ethane, ~2% propane, and <0.5% of higher hydrocarbons [24]. The cell was initially reduced in 100 sccm dry hydrogen during ramp up from room temperature to 800 °C. The peak power density was slightly lower than that reported previously for SLT-supported cells operated on methane [15]. Measurements of a number of cells suggested that power densities were similar in methane and natural gas; the lower power in Fig. 6a was due to cell-to-cell variations. On the other hand, the SLT cells typically yielded ~15% lower peak power density in natural gas compared to hydrogen fuel. This was previously explained by the relatively low amount of hydrogen present

in the anode due to the small amount of Ni catalyst in the SLT-supported cells, which limited hydrogen production via reforming [15].

In prior reports, short-term constant current tests have been used to explore the stable operating range for hydrocarbon-fuelled SOFCs [12,15,25]. Generally speaking, the SOFCs operate stably unless anode coking occurs. After the cell voltage had stabilized in dry hydrogen at 800 °C at a current density of 1.2 A cm^{-2}, the fuel was switched to 25 sccm dry natural gas. Fig. 6b shows such results with the cell operated in natural gas at fixed current density J for >8 h, with J decreased in steps: 1.2, 0.8, 0.45, and 0.2 A cm^{-2}. The cell performance remained stable at each J. The cell voltages measured at these current densities at the beginning of the test are labeled in Fig. 6a; this illustrates that the cell was stable, e.g., remaining at 0.85 V at 0.2 A cm^{-2}, throughout the test. For comparison, a Ni–YSZ-supported cell operated in this natural gas composition degraded rapidly due to coking even at a relatively high current density of 1.4 A cm^{-2}. The present results are similar to the wide stability range observed for these SLT cells operated with pure methane fuel [15]. The good stability was explained by the barrier-layer action of the SLT support, which trapped cell reaction products (H_2O and CO_2) and decreased the methane partial pressure in the thin Ni-based anode active layer, thereby avoiding coking conditions. A
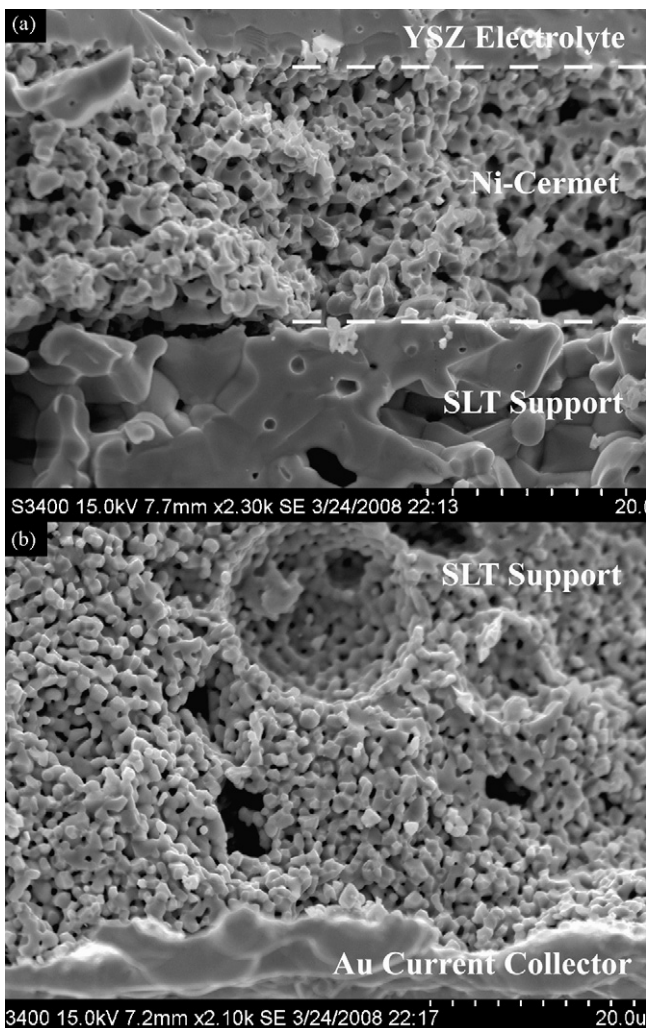
Fig. 7. Fracture cross-sectional images of an SLT-supported SOFC after operation on natural gas. Part (a) shows the region around the Ni–YSZ and Ni–SDC layers and (b) shows the SLT free surface.

Fig. 8. SEM-EDS spectra after SOFC testing in natural gas, from (a) the support/functional-layer interface of an SLT cell, (b) the free anode surface of an SLT-supported cell and (c) the free anode surface of a Ni–YSZ-supported cell.

detailed calculation showed that for a current density of 1 A cm^{-2} and a methane flow rate of 20 sccm, the O/C ratio at the Ni–YSZ anode layer was >1, outside of the range where coking is expected [15]. A similar explanation can be applied to the present natural gas results.

Overall, the cell voltage at 800 °C was stable for >80 h during these measurements in natural gas. Visual examination after the test showed no coking or visible deterioration of the SLT support surface, although there was coking on fuel gas-feed-tube surfaces. Fracture cross-sectional SEM imaging and EDS analysis of the cell were also carried out after the electrical tests shown in Fig. 6b. Fig. 7a shows an image of the region around the NiO–SDC barrier and NiO–YSZ active layer, where the structure looked identical to that of a cell tested in hydrogen. The EDS spectrum from this region (Fig. 8a) showed no evidence of carbon. Fig. 7b shows a typical

region near the free surface of the SLT support where there were no apparent effects of the natural gas operation on the structure, except in one of several images that showed an isolated ~6 µm carbon particle in one of the large SLT pores. The EDS spectrum (Fig. 8b) showed no carbon except at this one location.

For comparison, Fig. 8c shows the SEM-EDS spectrum obtained from the free anode surface of a Ni–YSZ-supported cell that was first reduced and stabilized in humidified H_2 and then operated at 800 °C in dry natural gas for 3 h. A strong carbon peak was observed. Images of Ni–YSZ-supported cells operated in natural gas showed substantial microstructure degradation due to coking, similar to that reported previously for methane [25]. These results verify that the degradation of Ni–YSZ-supported SOFCs operated in natural gas, shown in Fig. 6b, was due to coking.

3.5. Redox cycling

In Ni–YSZ-supported SOFCs, the cell performance degrades continuously with increasing number of redox cycles, i.e., alternating exposures of the anode to reducing (fuel) and oxidizing (air) conditions [26–28]. The redox cycling can lead to YSZ electrolyte fracture [29]. Fig. 9 shows an example of a seven-redox-cycle test of an SLT-supported SOFC. The results show excellent redox stability, as the cells returned to the same voltage after each air exposure. SEM images taken after redox cycling did not show any discernable structure change compared to cell operated under steady-state conditions (see Fig. 2). This may be due in part to the relatively low Ni:YSZ volume ratio of 0.54 (equal weights of NiO and YSZ in the anode). However, similar results were reported for segmented-in-series SOFCs [30], which also featured thin Ni–YSZ active layers on oxide supports, but with a higher Ni:YSZ volume ratio of 1.22. Thus, the redox cycling capability of the present cells can be attributed to the thin Ni–YSZ layer compared with Ni–YSZ-supported cells. Thermomechanical calculations suggest that the thin YSZ electrolyte is less susceptible to fracture upon redox cycling volume changes in a thin Ni–YSZ functional layer on an oxide support, compared to a thick Ni–YSZ support [31]. Previous reports have suggested that volume changes in SLT supports may be too large to allow stable redox cycling [17,32], but the present results show that this is not the case.
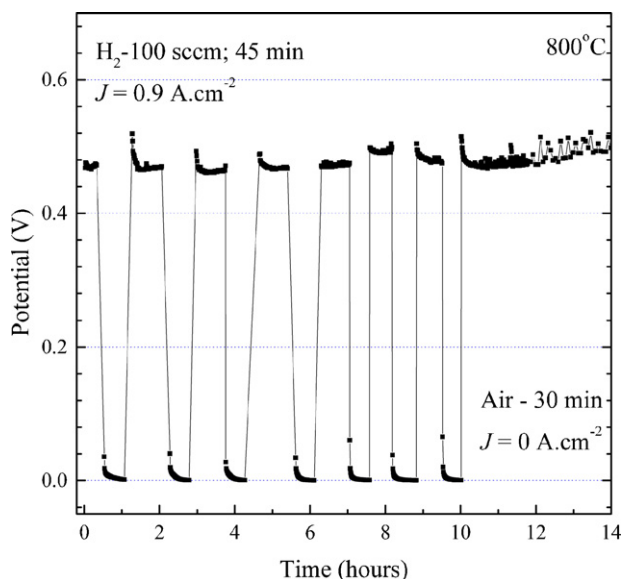

Fig. 9. Time dependence of cell voltage of an SLT-supported cell during a series of redox cycles where the cell was alternately exposed to dry H_2 for 45 min and air for 30 min.

Note that the previously measured SLT dimensional changes of $\geq 1\%$ were for samples exposed to air after initial firing at ≥ 1000 °C at low oxygen partial pressure. The change may be significantly less in the present SLT materials that were fired in air and cycled between air and dry hydrogen at ~800 °C.

4. Summary and conclusions

Solid oxide fuel cells with $Sr_{0.8}La_{0.2}TiO_3$ anode-side supports, along with Ni–YSZ anode, YSZ electrolyte, and LSM–YSZ cathode, were studied. The present SLT-supported SOFCs showed much-improved stability against coking in natural gas, compared with conventional Ni–YSZ anode-supported SOFCs. There was no long-term degradation in H_2S-contaminated fuel, and no degradation during redox cycling. While similar fuel flexibility (and in some cases better sulfur tolerance) can be achieved by using anodes where Ni is replaced by either Cu or an oxide conductor [1,3–7,33–35], the present SOFC design provides a fuel-flexible alternative that can be fabricated using conventional ceramic methods, has a standard anode-supported design, and yields relatively high power densities by utilizing a Ni–YSZ anode.

The present structures could also provide a basis for anode-supported cells with Ni-free anodes, by chemically etching away the Ni in the Ni-based layers and then infiltrating a conducting oxide active anode material. In such structures, the infiltrate electrical conductivity need only be sufficient for conduction across the thin (~30 µm) anode active layer to the conductive SLT support; for example, an active-layer conductivity of 0.3 S cm^{-1} would yield a relatively small ASR contribution of 0.01 Ω cm^2. Such structures could combine the excellent functionality of oxide anode active-layer materials with the relatively high power density of anode-supported SOFCs.

References

[1] A. Atkinson, S.A. Barnett, R.J. Gorte, J.T.S. Irvine, A.J. McEvoy, M.B. Mogensen, S. Singhal, J. Vohs, Nat. Mater. 3 (2004) 17–27.
[2] B.D. Madsen, M. Kobsiriphat, L.D. Marks, Y. Wang, S.A. Barnett, in: K. Eguchi, S.C. Singhal, H. Yokokawa, J. Mizusaki (Eds.), Proceedings of the SOFC X, Nara, Japan, 2007, pp. 1339–1348.
[3] B.D. Madsen, W. Kobsiriphat, Y. Wang, L.D. Marks, S.A. Barnett, J. Power Sources 166 (2007) 64–67.
[4] S. McIntosh, R.J. Gorte, Chem. Rev. 104 (2004) 4845–4865.
[5] Y.-H. Huang, R.I. Dass, Z.-L. Xing, J.B. Goodenough, Science 312 (2006) 254–257.
[6] S. Tao, J.T.S. Irvine, J. Electrochem. Soc. 151 (2004) A252–A259.
[7] O.A. Marina, L.R. Pederson, in: J. Huijismans (Ed.), Proceedings of the Seventh European SOFC Forum, Lucerne, Switzerland, 2002, p. 841.
[8] K. Ahn, S. Jung, J.M. Vohs, R.J. Gorte, Ceram. Int. 33 (2007) 1065–1070.
[9] S. Jung, C. Lu, H. He, K. Ahn, R.J. Gorte, J.M. Vohs, J. Power Sources 154 (2006) 42–50.
[10] H. Kurokawa, L. Yang, C.P. Jacobson, L.C. De Jonghe, S.J. Visco, J. Power Sources 164 (2007) 510–518.
[11] Z. Zhan, S.A. Barnett, Solid State Ionics 176 (2005) 871–879.
[12] Y. Lin, Z. Zhan, S.A. Barnett, J. Power Sources 158 (2006) 1313–1316.
[13] H. Zhu, A.M. Colclasure, R.J. Kee, Y. Lin, S.A. Barnett, J. Power Sources 161 (2006) 413–419.
[14] H. Zhu, A.M. Colclasure, R.J. Kee, Y. Lin, S.A. Barnett, in: U. Bossel (Ed.), Proceedings of the Seventh European SOFC Forum, Lucerne, Switzerland, 2006, p. B074.
[15] M.R. Pillai, Y. Jiang, N. Mansourian, I. Kim, D.M. Bierschenk, H. Zhu, R.J. Kee, S.A. Barnett, Electrochem. Solid State Lett., in press.

[16] M.D. Gross, J.M. Vohs, R.J. Gorte, Electrochem. Solid State Lett. 10 (2007) B65–B69.

[17] O.A. Marina, N.L. Canfield, J.W. Stevenson, Solid State Ionics 149 (2002) 21–28.

[18] S. Hashimoto, L. Kindermann, P.H. Larsen, F.W. Poulsen, M. Mogensen, J. Electroceram. 16 (2006) 103–107.

[19] S. Hashimoto, L. Kindermann, F.W. Poulsen, M. Mogensen, J. Alloy Compd. 397 (2005) 245–249.

[20] T. Tsai, S.A. Barnett, Solid State Ionics 98 (1997) 191.

[21] S. Zha, Z. Cheng, M. Liu, J. Electrochem. Soc. 154 (2007) B201–B206.

[22] H. Kurokawa, T.Z. Sholklapper, C.P. Jacobson, L.C.D. Jonghe, S.J. Visco, Electrochem. Solid State Lett. 10 (2007) B135–B138.

[23] Y. Matsuzaki, I. Yasuda, Solid State Ionics 132 (2000) 261–269.

[24] J.N. Armor, Appl. Catal. A: Gen. 176 (1999) 159–176.

[25] Y. Lin, Z. Zhan, J. Liu, S.A. Barnett, Solid State Ionics 176 (2005) 1827–1835.

[26] N. Tikekar, T. Armstrong, A. Virkar, J. Electrochem. Soc. 153 (2006) A654–A663.

[27] G. Stathis, D. Simwonis, F. Tietz, A. Moropoulou, A. Naoumides, J. Mater. Res. 17 (2002) 951–958.

[28] D. Waldbillig, A. Wood, D.G. Ivey, J. Power Sources 145 (2005) 206–215.

[29] J. Malzbender, E. Wessel, R.W. Steinbrech, Solid State Ionics 176 (2005) 2201–2203.

[30] M.R. Pillai, D. Gostovic, I. Kim, S.A. Barnett, J. Power Sources 163 (2007) 960–965.

[31] D. Sarantaridis, A. Atkinson, Fuel Cells 7 (2007) 246–258.

[32] F. Tietz, Q. Fu, V.A.C. Haanappel, A. Mai, N.H. Menzler, S. Uhlenbruck, Int. J. Appl. Ceram. Technol. 4 (2007) 436–445.

[33] B.D. Madsen, S.A. Barnett, J. Electrochem. Soc. 154 (2007) B501–B507.

[34] Z. Cheng, S. Zha, M. Liu, J. Electrochem. Soc. 153 (2006) A1302–A1309.

[35] S. Zha, P. Tsang, Z. Cheng, M. Liu, J. Solid State Chem. 178 (2005) 1844–1850.